Structure of Protein Cage Supercrystals Revealed by Angular X-ray Cross-Correlation Analysis

Kuan Hoon Ngoi, Laurin Lang, Young Yong Kim, Niklas Mucke, Gerard N. Hinsley, Dongwon Kim, Michael Rütten, Lars Klemeyer, Maximilian Ruffer, Varnika Yadav, Henrike Wagler, Tobias Katenkamp, Markus Perbandt, Azat Khadiev, Dmitri Novikov, Tobias Beck,* and Ivan A. Vartanyants*

Biohybrid supercrystals are highly ordered 3D assemblies of protein nanocages, offering versatile structural designs through the selection of protein nanocages and their ability to encapsulate various cargos within their cavities. By loading nanoparticles into these nanocages, diverse and complex superstructures can be engineered. In this study, individual biohybrid supercrystals are investigated using small-angle X-ray diffraction. As the samples may consist from single to several crystalline grains, angular X-ray cross-correlation analysis is used to analyze the angular correlations within the intensity distribution in 3D reciprocal space, enabling the determination of the unit cell parameters of the superlattice. Encapsulated nanoparticles serve as effective X-ray scattering markers, facilitating precise identification of the nanocage positions within the superlattice. The arrangement of nanoparticles in the unit cell is validated by comparing the experimental and calculated radial intensity profiles. The findings confirm the superlattice structures of unitary protein-nanoparticle composites, binary composites (including homobinary and heterobinary designs), and supercrystals with core-shell morphologies. Furthermore, single-grain and twin-domain structures are identified, demonstrating the capability of this technique for defect characterization and crystal engineering.

1. Introduction

The self-assembly of nanoparticles into 3D structures creates materials with emergent electronic, magnetic, plasmonic, and photonic properties, by harnessing the particles' unique properties and the synergistic interactions between them.[1,2] In this manner, materials are synthesized with properties that do not occur naturally, also known as metamaterials.[3] Methods for achieving controlled nanoparticle assembly include DNA-functionalized nanoparticles, where sequence-specific hybridization directs the arrangement of particles into well-defined structures.[4–7] Similarly, nanoparticles functionalized with charged organic ligands can be self-assembled through electrostatic interactions.[8–10] Another approach uses depletion forces, where an excluded volume effect induces attractive interactions between colloidal particles,[11] leading to their assembly into ordered superlattices.[12] However, the inherent polydispersity of inorganic nanoparticles makes the precise positioning within 3D structure challenging. Therefore, a precise matrix is required for the accurate positioning of the cargo particles within the materials. Here, protein nanocages offer an atomically defined building block for the organization of nanoparticles. Protein nanocages are hollow spheres with diameters in the nanoscale regime, usually from about 5 nm up to 50 nm, constructed by the assembly of a defined number of protein

K. H. Ngoi, G. N. Hinsley, A. Khadiev, D. Novikov, I. A. Vartanyants
Photon Science, Deutsches Electronen-Synchrotron DESY
Deutsches Elektronen-Synchrotron DESY
Notkestr. 85, 22607 Hamburg, Germany
E-mail: ivan.vartaniants@desy.de

L. Lang, N. Mucke, M. Rütten, L. Klemeyer, M. Ruffer, V. Yadav, H. Wagler, T. Katenkamp, M. Perbandt, T. Beck
Institute of Physical Chemistry
Department of Chemistry
University of Hamburg
Grindelallee 117, 20146 Hamburg, Germany
E-mail: tobias.beck@uni-hamburg.de

L. Lang, M. Ruffer, T. Beck
Hamburg Centre for Ultrafast Imaging
University of Hamburg
Luruper Chaussee 149, 22761 Hamburg, Germany

Y. Y. Kim, D. Kim
Beamline Division
Pohang Accelerator Laboratory
POSTECH
Pohang 37673, Republic of Korea

**ADVANCED
SCIENCE NEWS**

www.advancedsciencenews.com

**small
structures**

www.small-structures.com

subunits.[13] Protein cages are highly symmetric, usually displaying tetrahedral, octahedral, or icosahedral symmetry,[14,15] and have a cavity for loading with cargo. The cages can be filled with a range of nanoparticles,[16–18] either by in situ synthesis of the particles or by encapsulating pre-synthesized nanoparticles through a dis- and reassembly approach.[19,20] By loading protein nanocages with small molecules, biocompatible vehicles for drug delivery are produced.[21–23] Importantly, natural protein nanocages can be engineered or modified for improved loading, labeling, and delivery.[24,25] Moreover, with the recent advances in computational protein design, novel protein cage-like assemblies have been created.[26,27]

Protein nanocages as well-defined building blocks for materials can overcome the previously discussed polydispersity of nanoparticles during assembly. By using protein cages, we have recently established a novel approach for the self-assembly of nanoparticles.[28] Specifically, engineered protein nanocages with opposite surface charges are used as atomically precise templates for organizing inorganic nanoparticles. This methodology has demonstrated exceptional capabilities in generating binary nanoparticle superlattices with unprecedented structural accuracy and lateral dimensions. Because the nanocages and not the nanoparticles are the primary building blocks, different types of cargo loadings, for example, nanoparticles but also molecules such as dyes, can be realized for the 3D materials. The protein cages are assembled through electrostatic interactions between proteins with oppositely charged surfaces[28,29] or via metal coordination bridges between proteins with negatively charged surfaces.[20] By combining different types of redesigned protein nanocages, we created novel binary assemblies of differently sized nanoparticles.[30] Seminal work from other groups have co-assembled unmodified protein cages and charged gold nanoparticles (AuNPs),[31] oppositely charged natural proteins,[32] and utilized unitary protein cage lattices filled with two types of enzymes as cargo for multistep catalysis.[33] Assemblies containing protein-protein cage hybrid have been created as well.[34] Interestingly, other groups have utilized the approach developed in our group of using two oppositely charged protein nanocages, with one building block being the supercharged ferritin Ftn$^{(pos)}$,[28] to create other types of binary nanoparticle assemblies and study the interaction of nanoparticles within the lattices.[35] One current focus of assembly is the creation of core-shell morphologies, where protein cages have been utilized to synthesize a multi-layered ordered array[36] and core-shell crystals.[37] Through DNA-mediated assembly, core-shell superlattices were created as well.[38]

In recent studies, we have explored the optical properties of biohybrid superlattices based on protein nanocages: encapsulation of AuNPs and fluorophores has produced optical nanomaterials exhibiting strong exciton-plasmon interactions.[39] Furthermore, we have constructed superlattices based on protein nanocages and AuNPs to demonstrate novel optical phenomena such as anomalous refraction of visible light.[40] The cavities within the protein cages can be loaded in a modular fashion with a range of inorganic nanoparticles such as metal oxide or noble metal nanoparticles, enabling the development of diverse biohybrid superlattice architectures.[28,29,39,40]

Compared to other methods for self-assembly discussed above, the approach of using protein cages for assembly has strengths and weaknesses. For example, there is a high long-range order of the superlattices due to the protein cage providing

an atomically defined template. By fixating the final assemblies, for example, with chemical crosslinkers, the crystals can be removed from the crystallization solution and further manipulated and investigated, even in vacuums. Due to the rather thin protein shell, a large fraction of the final material contains nanoparticles. However, the distances between particles cannot be tuned as readily as, for example, with DNA-based assembly, where the lattice constants can be controlled through variation in the DNA linker length. The control of lattice symmetry is important for future applications. Here, the pH value and the concentration of metal ions in the assembly condition can affect the type of protein cage lattice structure.[20,41] Another challenge is to incorporate differently sized nanoparticles. Ideally, various types of nanoparticles with different sizes should be integrated into these materials. However, adjusting the size of the protein nanocage is not straightforward and requires the use of different types of cages for the assembly. Because different types of cages show different types of symmetry, it is crucial to determine the arrangement of the cages in the condensed matter, for example the crystal type and lattice parameters. Such insights will allow for the controlled design of biohybrid superlattices with specific structures and thus properties.

In this study, we investigate biohybrid superlattices with a homogeneous distribution of nanoparticles and, for the first time for our systems, supercrystals with a core-shell morphology (for other studies, see for example refs. [36–38]). Because the crystal lattice does not depend on the cargo but only on the cages, we envisioned that the core-shell lattices form a similar crystal type compared to the parent lattice. We study superlattices organized by two types of protein nanocages, encapsulin (Enc) with a diameter of 24 nm and ferritin (Ftn) with a diameter of 12 nm (**Figure 1**). We utilize three protein cage variants: engineered and negatively charged, obtained by supercharging the parent protein cages encapsulin from *T. maritima* (Enc$^{(neg)}$) and two ferritin variants obtained by supercharging of human heavy chain ferritin to yield positively charged ferritin (Ftn$^{(pos)}$) and negatively charged ferritin (Ftn$^{(neg)}$). These cages encapsulate either AuNPs with a diameter of 12 nm or cerium oxide nanoparticles (CeO$_2$ NPs) with a diameter of 6 nm. The synthesis of CeO$_2$ NPs inside the ferritin cages was carried out according to an already reported approach.[20] For the AuNPs, a previously established protocol was used for encapsulation within Enc$^{(neg)}$ through a cargo-loading peptide (CLP)-mediated approach.[30] The loaded cages were characterized, for example, using transmission electron microscopy, which shows one nanoparticle per cage.[30] The cages function as a matrix and organize these cargo particles into micron-sized highly ordered 3D biohybrid superlattices, also referred to as biohybrid supercrystals (see for details in Experimental Section and Supporting Information).

This study provides a detailed investigation into the structural ordering and lattice parameters of protein-nanoparticle superlattices using small-angle X-ray diffraction (SAXD). By utilizing the X-ray scattering signals of encapsulated inorganic nanoparticles, which serve as effective markers for their encapsulating protein cages, the structural arrangement within the superlattices can be precisely probed. We use the angular X-ray cross-correlation analysis (AXCCA) to investigate the angular correlations in the intensity distribution within the reciprocal space of individual biohybrid supercrystals.[42–45] This approach proves useful for
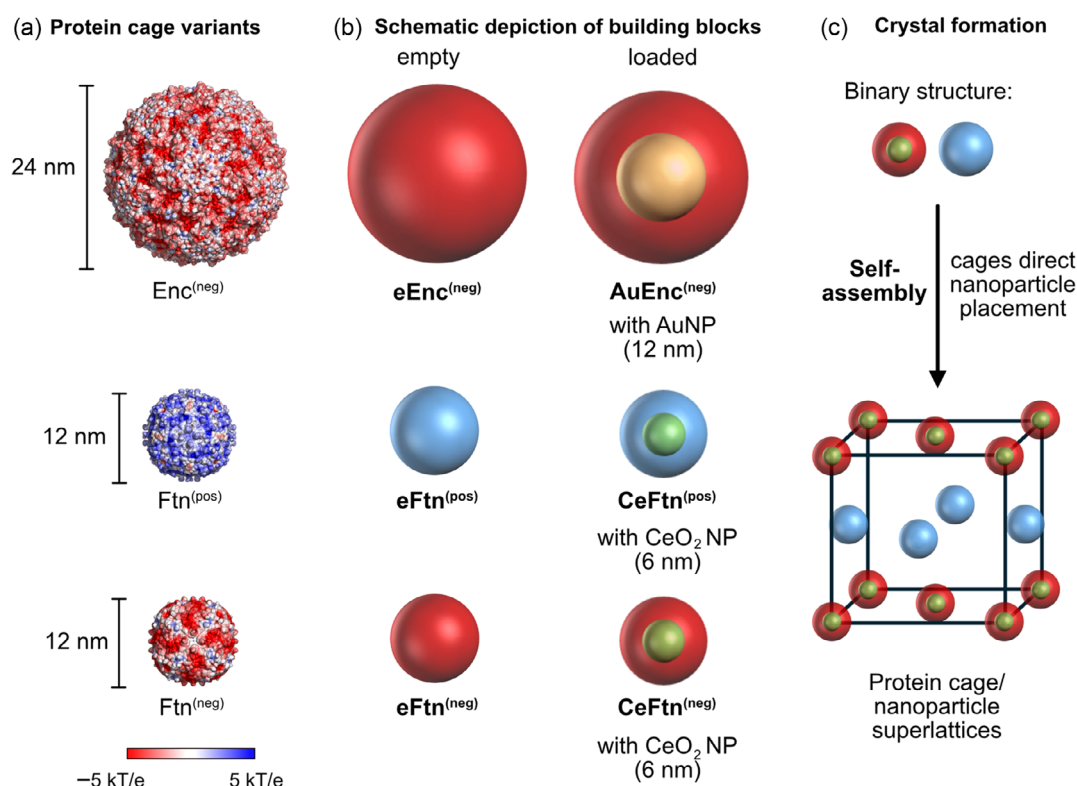
Figure 1. Building blocks and assembly of the biohybrid superlattices. a) Three different protein cages are used for the assembly of nanoparticles: negatively charged encapsulin (Enc$^{(neg)}$) from *T. maritima*, positively charged ferritin (Ftn$^{(pos)}$), and negatively charged ferritin (Ftn$^{(neg)}$) based on human heavy chain ferritin. The outer surface is either negatively charged (electrostatic potential depicted in red, -5 kT/e) or positively charged (blue, $+5$ kT/e). The cavity is used for nanoparticle encapsulation. b) Protein cages are either filled with nanoparticles such as AuNPs or CeO$_2$ NPs or used as empty cages for the assembly. c) Biohybrid superlattices are formed by the self-assembly of either two types of protein cages (shown here) or by the assembly of one type of protein cage filled with nanoparticles. These assemblies are referred to as binary or unitary protein-nanoparticle composites, respectively.

extracting the unit cell parameters across single to several crystalline domains[46,47] and identifying structural defects, such as grain boundaries,[48,49] stacking faults,[45,50,51] and twinned domains.[45,52] Additionally, the unit cell parameters allow the determination of diffraction positions, facilitating the identification of the spatial arrangement of nanoparticles within the unit cell by comparing the experimental and simulated peak intensities in the radially averaged scattering intensities.[53–55]

2. Results and Discussion

2.1. Overview of Biohybrid Supercrystals and Diffraction Data Collection

Biohybrid supercrystals based on protein nanocages and nanoparticles are classified into two primary categories based on the number of different protein cages used for assembly: unitary and binary protein-nanoparticle composites. The first category, unitary protein-nanoparticle composites, includes two configurations. First, there are negatively charged ferritin cages loaded with CeO$_2$ NPs, referred to as the CeFtn$^{(neg)}$ crystal. Second, there are negatively charged encapsulin cages containing AuNPs, referred to as the AuEnc$^{(neg)}$ crystal.

The second category, binary protein-nanoparticle composites, is more complex and includes both homobinary and heterobinary designs. The homobinary design involves ferritin cages with oppositely charged components (positive and negative). These are known as homobinary crystals because they utilize two protein cages derived from the same parent cage. Here, as an example, the negatively charged ferritin cages loaded with CeO$_2$ NPs and assembled with empty, positively charged ferritin cages, are referred to as the CeFtn$^{(neg)}$/eFtn$^{(pos)}$ crystal. In the heterobinary design, the scaffold consists of two distinct protein cages, namely negatively charged encapsulin cages and positively charged ferritin cages, Enc$^{(neg)}$ and Ftn$^{(pos)}$. There are two subtypes: the first subtype consists of negatively charged encapsulin cages loaded with AuNPs combined with positively charged, empty ferritin cages, referred to as the AuEnc$^{(neg)}$/eFtn$^{(pos)}$ crystal. The second subtype contains empty encapsulin cages paired with ferritin cages loaded with CeO$_2$ NPs, referred to as the eEnc$^{(neg)}$/CeFtn$^{(pos)}$ crystal. Microscopy images of the different types of biohybrid supercrystals investigated in the current study are shown in **Figure 2**.

Additionally, biohybrid supercrystals with a core-shell morphology were synthesized. Here, a seed crystal was first grown as the core and was then transferred to a solution containing the cage composites for the shell. Please note that the
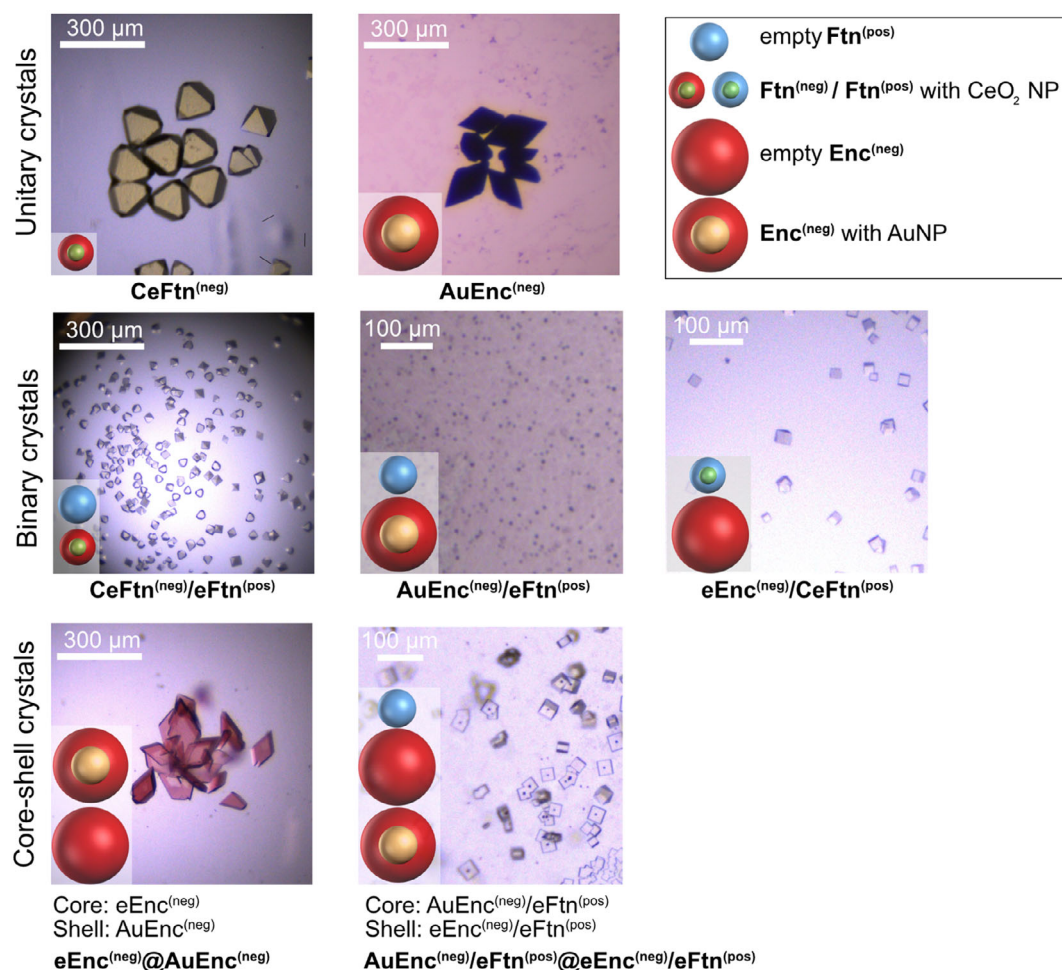
Figure 2. Optical microscopy images of supercrystals based on protein nanocages and nanoparticles. The insets show the building blocks for each crystal type (see also Figure 1) as well as the crystal type. The abbreviations in bold below each panel are used throughout the text to identify the crystal type.

composition of the crystal growth solution for the core and the shell contained the same type of cages, which were either filled with nanoparticles or left as empty cages (see the Experimental Section for more details). For crystals with the Enc$^{(neg)}$ architecture, the outer shell consists of encapsulin cages loaded with AuNPs, while the inner core contains only empty encapsulin cages, referred to as eEnc$^{(neg)}$@AuEnc$^{(neg)}$ crystal. For crystals based on Enc$^{(neg)}$/Ftn$^{(pos)}$ structure, the core is composed of encapsulin cages loaded with AuNPs and empty ferritin cages, whereas the outer shell is composed of layers of empty encapsulin and ferritin cages, referred to as the AuEnc$^{(neg)}$/eFtn$^{(pos)}$@eEnc$^{(neg)}$/eFtn$^{(pos)}$ crystal. We envisioned that by utilizing the cages as building blocks, the final core-shell assemblies should be very similar to the parent crystals, which have a homogeneous distribution of nanoparticles throughout the crystal.

To reveal the structure of these protein cage supercrystals, the SAXD experiment was performed at the in situ X-ray diffraction and imaging beamline P23 at PETRA III. A schematic layout of
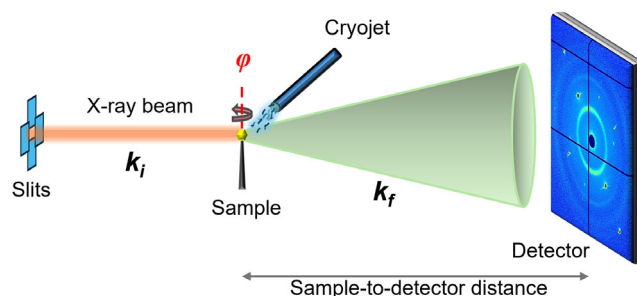
Figure 3. Scheme of the experimental setup for measuring 2D diffraction patterns from a biohybrid supercrystal. The sample was cooled using a liquid nitrogen cryojet to 100 K. Scattering patterns were acquired using a 2D detector placed downstream of the sample. The sample was rotated around the vertical axis (φ) over an angular range of 180°. The vectors k_i and k_f denote the incident and scattered wave vectors of X-rays. The sample-to-detector distance was different in the course of the experiment, where the detector was positioned at a distance of either 0.9 or 1.5 m.

**ADVANCED
SCIENCE NEWS**

www.advancedsciencenews.com

**small
structures**

www.small-structures.com

the experimental setup is shown in **Figure 3**. Individual biohybrid supercrystals were illuminated with X-rays at an energy of 12.5 keV in transmission geometry and were rotated around the vertical axis over an angular range to collect the full 3D intensity distribution. The 3D intensity distribution was further analyzed using AXCCA and further processed by orientational averaging to generate a 1D radial intensity profile for subsequent scattering analysis (see the Experimental Section for more details). In total, about five crystals were measured for each type of sample.

2.2. Unitary Protein-Nanoparticle Composites

We begin our discussion with the simple unitary protein-nanoparticle composites. The experimental radial intensity profiles for these composites were generated, with the vertical axis representing measured intensity and the horizontal axis corresponding to the magnitude of the scattering vector, q. These profiles are shown in **Figure 4**a for the CeFtn[neg] crystal and in Figure 4b for the AuEnc[neg] crystal, with the data presented as black circles. The intensity profiles exhibit multiple diffraction peaks attributed to the structure factor, along with intensity oscillations arising from the form factor of the encapsulated nanoparticles within the superlattice. The observed peaks are broad, with

some overlapping, and their intensities diminish with increasing momentum transfer value q. The overlap between structure factor and form factor contributions within the same q-regime results in the modulation of the diffraction peak intensities by the particle form factor, complicating the structure determination. These characteristics are observed consistently throughout the radial intensity profiles of all the supercrystals discussed in this study.

Separating the structure factor from the intensity profiles requires determining the particle form factor, which has been demonstrated by melting the thin film superlattice into a random arrangement[6] or by using a dilute colloidal solution with identical constituents.[56] However, these approaches are not suitable for the individual supercrystal samples. The former method is destructive, preventing subsequent post-characterization of the sample, while the latter does not ensure the nanoparticle form factor in solution accurately resembles that in the solid state. To overcome these limitations, we used AXCCA on the 3D intensity distribution of supercrystals for unit cell determination. AXCCA examines the angular correlations between pairs of scattering intensities with scattering vectors q_1 and q_2, respectively.[45] In this study, we consider pairs of intensities where the magnitudes are equal, $|q_1| = |q_2| = q$. The angular cross-correlation function (CCF) was calculated by averaging over all intensity pairs with a specific relative angle at a fixed q-value
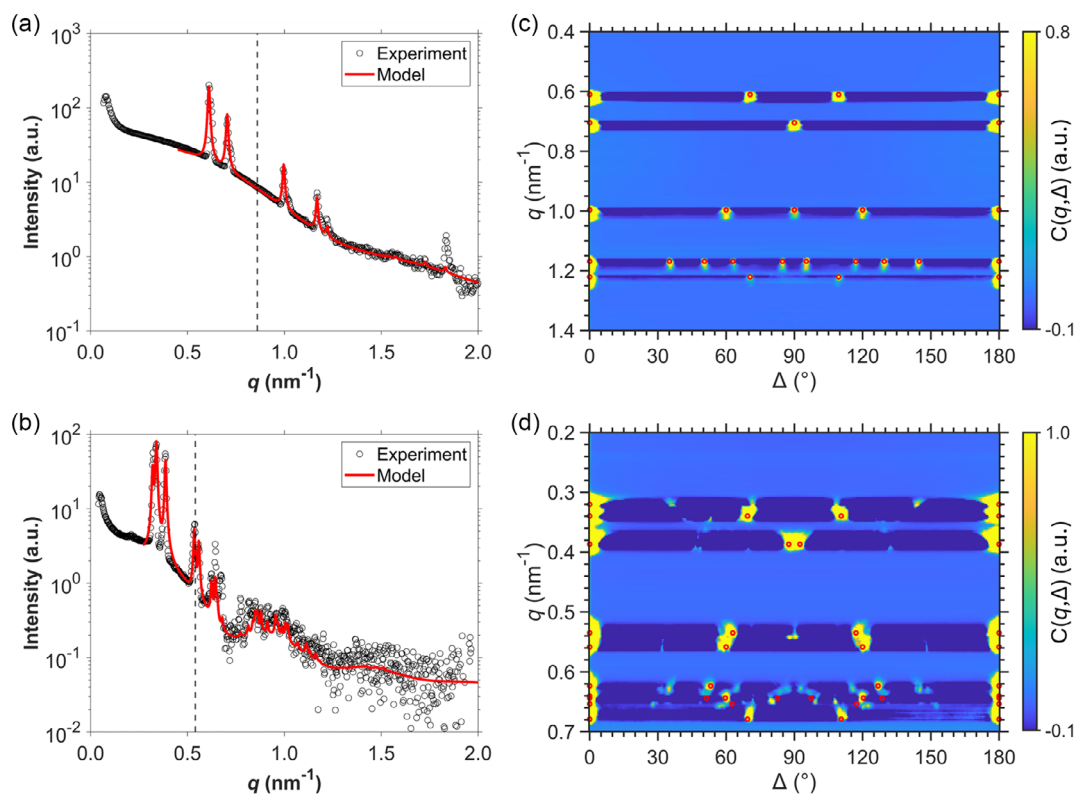
Figure 4. a,b) Radial intensity profiles for the CeFtn[neg] (a) and AuEnc[neg] (b) crystals. They are shown on a logarithmic scale as a function of the scattering vector magnitude, q. Experimental data are represented by black circles, and the vertical dashed line marks the maximum extent of the full q-circle ($q_{full} = q_x = q_y$) that can be captured by the detector. c,d) Correlation maps $C(q, \Delta)$ are displayed for the CeFtn[neg] crystal with a q-step size of 0.0037 nm^{-1} (c) and for the AuEnc[neg] crystal with a q-step size of 0.0023 nm^{-1} (d). The correlated positions (g_{hkl}, Δ_g) are calculated from the primitive rhombohedral lattice and marked as red circles in the correlation maps. Based on the determined unit cell parameters and the predicted nanoparticle arrangement, the radial intensity profiles were calculated and shown as red lines in the left panels.

(see details in the Experimental Section). This analysis not only suppresses the random angular correlations but also extracts the angular correlations of Bragg peaks within the 3D intensity distribution.

The angular CCFs were calculated from the 3D intensity distribution from a given q-regime and then stacked together to generate a 2D correlation map. In this map, the vertical axis represents the magnitude of the scattering vector q, the horizontal axis represents the relative angle Δ between intensity pairs, and the color map represents the calculated angular correlation values. Local maxima of these correlation peaks, characterized by coordinates (q_{obs}, Δ_{obs}), were subsequently identified and compared with the correlation positions (g_{hkl}, Δ_g) derived from the proposed model lattice with specific unit cell parameters (a, b, c, α, β, and γ). Here, g_{hkl} represents the magnitude of the reciprocal lattice vector, and Δ_g denotes the relative angle between a pair of the reciprocal lattice vectors (see Supporting Information for further details). This approach provides the unit cell parameters of the biohybrid superlattice, offering basic structural information necessary for understanding the organization of the protein-nanoparticle building blocks within the supercrystal.

To investigate the superlattice structure within unitary protein-nanoparticle composites, we calculated the angular CCFs from the 3D intensity distribution for the CeFtn$^{(neg)}$ crystal (Figure 4c) and for the AuEnc$^{(neg)}$ crystal (Figure 4d). Unit cell determination revealed that the nanoparticles in the supercrystals exhibit a primitive rhombohedral superlattice structure ($a_R = b_R = c_R$, $\alpha_R = \beta_R = \gamma_R$). The experimental correlation peaks on the CCF maps align closely with those calculated for the model lattice, as indicated by the red circles, suggesting that this crystal is a well-formed, single-grain structure. The determined unit cell parameters are listed in **Table 1**.

In detail, the CeFtn$^{(neg)}$ crystal consists of negatively charged ferritin cages loaded with CeO$_2$ NPs. They assemble into a primitive rhombohedral lattice with unit cell parameters $a_R = 12.61$ nm and $\alpha_R = 60.00°$ (as illustrated in **Figure 5**a). It has been reported that the repulsive force between like-charged ferritins is mitigated by magnesium ions absorbed at their interface, facilitating the assembly of these like-charged ferritins into the superlattice.[20] Correspondingly, the primitive rhombohedral unit cell with $\alpha_R = 60.00°$ can also be represented as a face-centered cubic (fcc) unit cell (Figure 5b), with the unit cell parameters $a_C = \sqrt{2}a_R = 17.83$ nm and $\alpha_C = 90.00°$. This configuration forms a close-packed structure, with the close-packed direction aligned along <111> direction of the unit cell.

Table 1. Structural parameters for the optimized model of the CeFtn$^{(neg)}$ and AuEnc$^{(neg)}$ crystals obtained through the AXCCA. The mean values of the unit cell parameters for the nanoparticle superlattices were determined from the AXCCA, with the error bars representing the standard deviation determined by the Williamson–Hall method.

Sample name	CeFtn$^{(neg)}$	AuEnc$^{(neg)}$
Unit cell length, a_R [nm]	12.61 ± 0.27	23.58 ± 0.49
Unit cell angle, α_R [°]	60.00 ± 0.59	57.21 ± 1.50
Nearest neighbor distance, d_{NN} [nm]	12.61 ± 0.27	22.58 ± 0.47
Type of unit cell	Rhombohedral	Rhombohedral
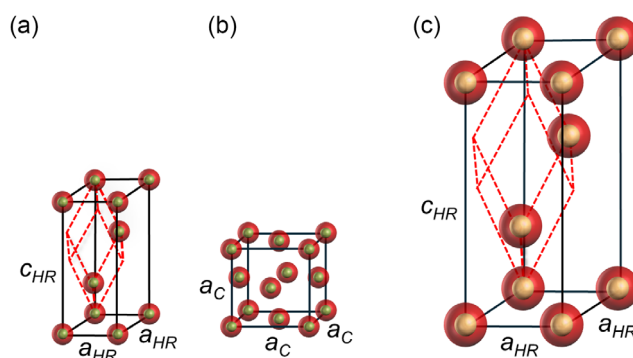
Figure 5. Schematic view of the unitary protein-nanoparticle lattices and their corresponding unit cells is shown for the CeFtn$^{(neg)}$ crystal: a) in a rhombohedral unit cell with hexagonal axes and b) in an fcc unit cell. Additionally, c) shows the AuEnc$^{(neg)}$ crystal in the rhombohedral unit cell with hexagonal axes. The red dashed lines in (a) and (c) depict primitive rhombohedral unit cells.

On the other hand, the AuEnc$^{(neg)}$ crystal consists of negatively charged encapsulin loaded with Au nanoparticles,[19] arranged into a primitive rhombohedral lattice with unit cell parameters $a_R = 23.58$ nm and $\alpha_R = 57.21°$ (Figure 5c). In the correlation map shown in Figure 4d, some correlation peaks are not explained by the correlation positions calculated from the model lattice. Since the α_R of the AuEnc$^{(neg)}$ crystal is close to 60.00°, which is a characteristic of a primitive rhombohedral unit cell of an fcc structure, this prompted further examination of possible defects associated with the fcc structure within this crystal. This investigation began by comparing both the CeFtn$^{(neg)}$ and AuEnc$^{(neg)}$ crystals in a rhombohedral-centered lattice with hexagonal axes ($a_{HR} = b_{HR}$, c_{HR}, $\alpha_{HR} = \beta_{HR}$, $\gamma_{HR} = 120°$), where $a_{HR} = a_R\sqrt{2 - 2\cos\alpha_R}$ and $c_{HR} = a_R\sqrt{3 + 6\cos\alpha_R}$ (see Figure 5a,c). For the CeFtn$^{(neg)}$ sample, $a_{HR} = 12.61$ nm and $c_{HR} = 30.89$ nm, while for the AuEnc$^{(neg)}$ sample, $a_{HR} = 22.63$ nm and $c_{HR} = 59.18$ nm. The nearest neighbor distance (d_{NN}) between adjacent protein cages in CeFtn$^{(neg)}$ and AuEnc$^{(neg)}$ crystals is located within the basal plane normal to [0001] and corresponds to a_{HR}.

In this configuration, each protein cage in the CeFtn$^{(neg)}$ crystal is coordinated with twelve neighboring cages, all with the same d_{NN}. Similarly, in the AuEnc$^{(neg)}$ crystal, each protein cage is coordinated with twelve neighboring cages. Six cages are within the same basal plane, all at the same d_{NN}, and an additional six cages, with three positioned above and three below the basal plane, each at a neighboring distance a_R, which is $\approx4.4\%$ greater than the d_{NN}. Assuming the size of each protein cage as d_{NN}, this results in a packing factor for the CeFtn$^{(neg)}$ crystal of ≈0.74, characteristic of a close-packed structures.[57] In contrast, the AuEnc$^{(neg)}$ crystal has a packing factor of 0.69, suggesting a looser packing density in the AuEnc$^{(neg)}$ crystal relative to the CeFtn$^{(neg)}$ crystal.

In addition, both crystals consist of a regular stacking sequence (ABCABC...) in the direction normal to the basal planes. Any disruption of the stacking sequence typically leads to the occurrence of twinning, a phenomenon frequently observed in fcc lattices.[58,59] This results in mirror symmetry of the twinned domains across the twin boundary parallel

to the basal planes. As shown in Figure S4a, Supporting Information, the previous unexplained correlation peaks in the map coincide with the correlation positions between two twinned grains, providing evidence for the presence of twin domains in the AuEnc(neg) crystal. The formation of these domains in the superlattice is likely initiated during the crystal growth process due to stacking faults or structural rearrangement.

After obtaining the unit cell parameters from the AXCCA, the peak positions of the structure factor were calculated. Using a scattering formalism derived from the periodic nanoparticle lattices, the scattering intensities of the proposed structural model can be computed,[53–55,60] with a detailed analysis available in the Supporting Information. This approach enables the examination of the predicted superlattice structure, including the unit cell parameters and the arrangement of encapsulated nanoparticles. The calculated intensity profile for CeFtn(neg) and AuEnc(neg) crystals, shown as red lines in Figure 4a,b, demonstrates a good agreement with the experimental data, particularly for the diffraction peak intensities. This consistency further supports the proposed superlattice structures of nanoparticles,
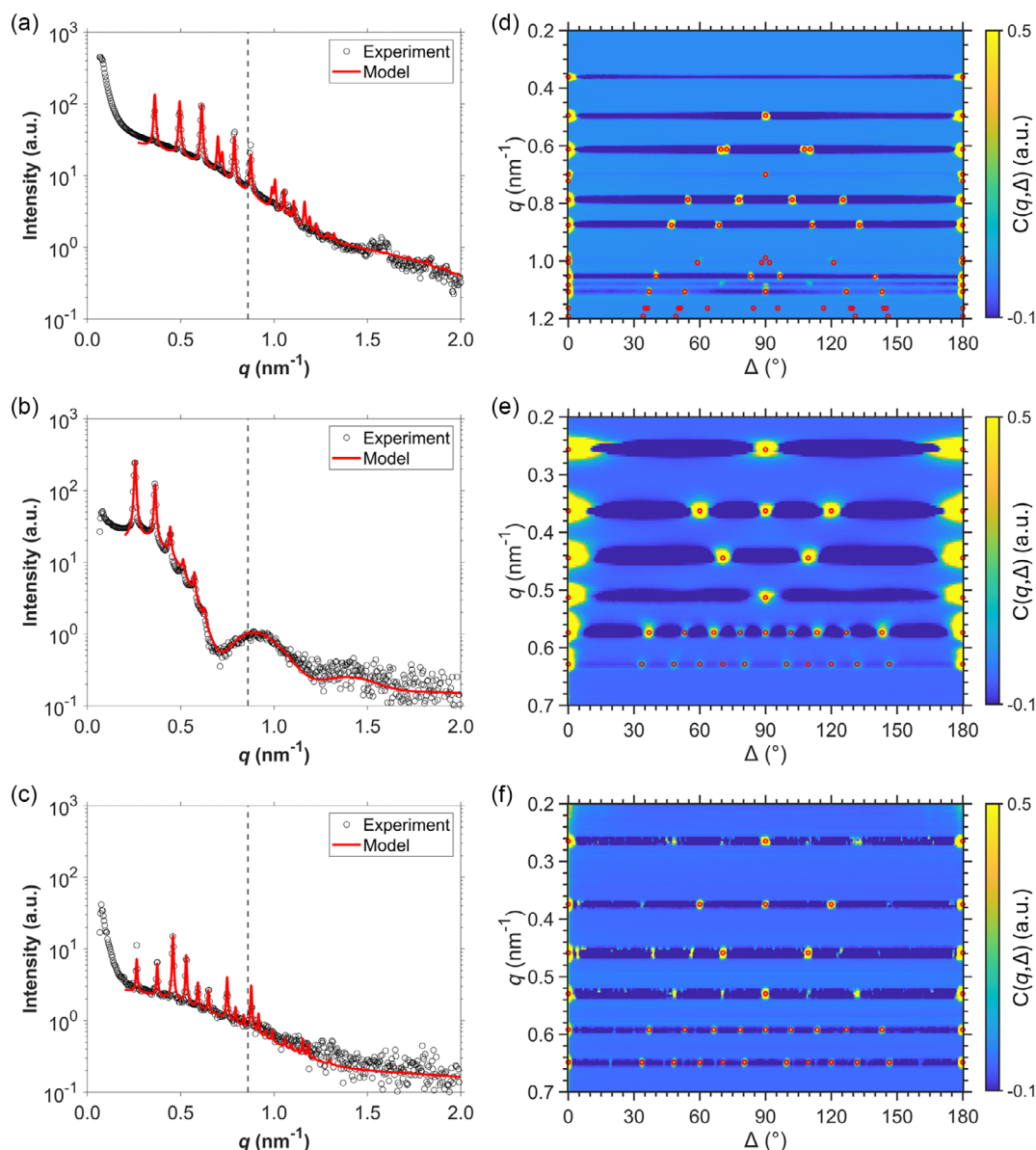
Figure 6. a–c) Radial intensity profiles for the CeFtn(neg)/eFtn(pos) (a), AuEnc(neg)/eFtn(pos) (b), and eEnc(neg)/CeFtn(pos) (c) crystals. They are shown on a logarithmic scale as a function of the scattering vector magnitude, q. Experimental data are represented by black circles, and the vertical dashed line marks the maximum extent of the full q-circle ($q_{full} = q_x = q_y$) measured by the detector. d–f) Correlation maps $C(q, \Delta)$ are displayed for the CeFtn(neg)/eFtn(pos) (d), AuEnc(neg)/eFtn(pos) (e), and eEnc(neg)/CeFtn(pos) (f) crystals with a q-step size of 0.0037 nm^{-1}. The correlated positions (g_{hkl}, Δ_g) are calculated from the model lattice and marked as red circles in the correlation maps. The CeFtn(neg)/eFtn(pos) crystal features a nanoparticle superlattice with a simple tetragonal structure, while the AuEnc(neg)/eFtn(pos) and eEnc(neg)/CeFtn(pos) crystals exhibit simple cubic structures. Using the determined unit cell parameters and the predicted nanoparticle arrangement, the radial intensity profiles were calculated and are shown as red lines in the left panels.

which correspond to their encapsulating protein cages within the biohybrid supercrystals.

2.3. Binary Protein-Nanoparticle Composites

We also studied three types of binary protein-nanoparticle composites: (i) the homobinary CeFtn(neg)/eFtn(pos) crystal, (ii) the heterobinary AuEnc(neg)/eFtn(pos) crystal, and (iii) the heterobinary eEnc(neg)/CeFtn(pos) crystal. The collected intensity distributions were averaged into radial intensity profiles, as shown in **Figure 6**a–c. Correlation maps were calculated from these intensity distributions for the CeFtn(neg)/eFtn(pos) crystal (Figure 6d), for the AuEnc(neg)/eFtn(pos) crystal (Figure 6e), and the eEnc(neg)/CeFtn(pos) crystal (Figure 6f). The analysis revealed distinct nanoparticle superlattice structures for each composite: the CeFtn(neg)/eFtn(pos) crystal forms a simple tetragonal lattice ($a_T = b_T$, c_T, $\alpha_T = \beta_T = \gamma_T = 90°$), while the AuEnc(neg)/eFtn(pos) and eEnc(neg)/CeFtn(pos) crystals form simple cubic lattices ($a_L = b_L = c_L$, $\alpha_L = \beta_L = \gamma_L = 90°$). The correlation peaks on the map of the CeFtn(neg)/eFtn(pos) and AuEnc(neg)/eFtn(pos) crystals coincide with those calculated for the model lattice, as indicated by the red circles, suggesting that both crystals exist as a single-grain crystal. However, this is not the case for the eEnc(neg)/CeFtn(pos) crystal, which shows multiple unexplained peaks. The unit cell parameters determined from this analysis are provided in **Table 2**.

For the CeFtn(neg)/eFtn(pos) crystal, negatively charged ferritin cages loaded with CeO_2 NPs assemble in a simple tetragonal lattice with unit cell parameters $a_T = 12.73$ nm and $c_T = 17.43$ nm. The a_T represents the distance between two negatively charged ferritin cages at the corners of the unit cell; the body diagonal length was determined to be 25.06 nm, nearly twice the value of a_T. This suggests the presence of positively charged ferritin cages at the body-centered site of the unit cell, consistent with the previous finding.[20] It was reported that the like-charged

Table 2. Structural parameters for the CeFtn(neg)/eFtn(pos), AuEnc(neg)/eFtn(pos), and eEnc(neg)/CeFtn(pos) crystals obtained through the AXCCA. The mean values of the unit cell parameters for the nanoparticle superlattices were determined from the AXCCA, with the error bars representing the standard deviation determined by the Williamson–Hall method.

Sample name	CeFtn(neg)/ eFtn(pos)	AuEnc(neg)/ eFtn(pos)	eEnc(neg)/ CeFtn(pos)
Unit cell length, a_L [nm]	18.00 ± 0.23	24.49 ± 0.38	23.73 ± 0.34
Unit cell length, c_L [nm]	17.43 ± 0.22	–	–
Unit cell angle, α_L [°]	90.00 ± 0.78	90.00 ± 1.19	90.00 ± 0.76
Nearest neighbor distance between two ferritins, $d_{NN, Ftn}$ [nm]	12.53 ± 0.14	17.31 ± 0.24	16.78 ± 0.24
Nearest neighbor distance between two encapsulins, $d_{NN, Enc}$ [nm]	–	24.49 ± 0.38	23.73 ± 0.34
Type of unit cell	simple tetragonal	simple cubic	simple cubic

ferritin cages assemble into a superlattice described by a simple tetragonal unit cell, with the body-centered site occupied by an oppositely charged ferritin cage. Half of the body diagonal length is 12.53 nm, which is slightly smaller than a_T, indicating a reduced distance between oppositely charged ferritins in the unit cell. This difference is attributed to electrostatic interactions between the charged ferritins. The reported structure is also analogous to an AB alloy with a tetragonal $L1_0$ ordered structure (a fcc-derived ordered structure, exhibiting unit cell parameters $a_L = \sqrt{2}a_T = 18.00$ nm and $c_L = c_T = 17.43$ nm (**Figure 7**a). This corresponds to a ratio c_L/a_L of 0.968, comparable to the ordered CoPt intermetallic compound.[61] The calculated radial intensity profile from the proposed structure matches the experimental data, shown as a red line in Figure 6a.
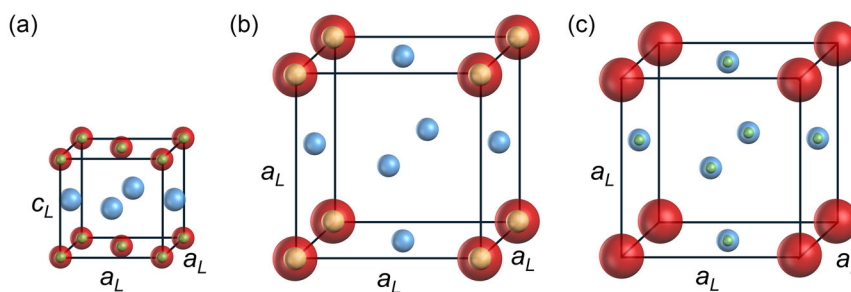
For the heterobinary protein-nanoparticle composites, the analysis of the AuEnc(neg)/eFtn(pos) crystal reveals that AuNPs encapsulated in negatively charged encapsulin cages organize into a simple cubic lattice with the unit cell parameter $a_L = 24.49$ nm, suggesting that the large encapsulin cages only occupy the corners of the cubic unit cell. Its counterpart, the eEnc(neg)/CeFtn(pos) crystal, composed of negatively charged ferritin cages loaded with CeO_2 NPs, also adopts a simple cubic lattice with a smaller unit cell parameter $a_L = 23.73$ nm. To estimate the site occupancy of ferritins within the unit cell, ferritin and encapsulin are modeled as rigid spheres, with sizes corresponding to the d_{NN} found in the CeFtn(neg) and AuEnc(neg) crystals, representing the smallest sizes possible of the respective cages. Subtracting the rigid AuEnc(neg) sphere from the face and body diagonals of the unit cell estimates unoccupied distances of 10.98 nm along the face diagonal and 18.52 nm along the body diagonal of the eEnc(neg)/CeFtn(pos) crystal, available for potential ferritin cage occupancy. Similarly, the unoccupied distances along the face and body diagonals of the unit cell in the AuEnc(neg)/eFtn(pos) crystal are 12.05 and 19.84 nm, respectively.

Subsequently, three possible configurations for the site occupancy of ferritin cages in the unit cell were further evaluated. First is an AB_3 structure (cubic $L1_2$ ordered structure) with ferritin cages positioned at the face-centered sites of the unit cell. Second is a CsCl structure, where ferritin cages are positioned at the body-centered sites of the unit cell. Last is an AB_4 structure, as examined in the previous findings,[30] with the ferritin cages located at both the body-centered and face-centered sites of the unit cell. By comparing the experimental and calculated radial intensity profiles, the AB_3-type structure showed the best match, compared to the AB_4-type structures (see Figure S5a, Supporting Information) and CsCl structures (see Figure S5b, Supporting Information). These results suggest that ferritin cages occupy the face-centered sites and encapsulin cages occupy the corners of the unit cell. Therefore, both AuEnc(neg)/eFtn(pos) and eEnc(neg)/CeFtn(pos) crystals adopt a cubic $L1_2$ ordered structure (as shown in Figure 7b,c). These findings are consistent with recent studies using cryogenic transmission electron microscopy and tomography,[30] which revealed that this composite assembles into an AB_3-type superlattice, similar to the ordered Cu_3Au intermetallic compound. Nonetheless, given that the ferritin cages are slightly larger than the unoccupied space at the face-centered sites, positioning them at these sites introduces weak geometric frustration within the superlattice structure.

ADVANCED
SCIENCE NEWS

www.advancedsciencenews.com

small
structures

www.small-structures.com

Figure 7. a–c) Schematic view of the binary protein-nanoparticle lattices with the corresponding unit cell. The protein cages assembled into a tetragonal L1$_0$ ordered structure and nanoparticle superlattice form a simple tetragonal structure for the CeFtn$^{(neg)}$/eFtn$^{(pos)}$ crystal (a). The protein cages assembled in a cubic L1$_2$ ordered structure, with the nanoparticle superlattice forming a simple cubic structure both for the AuEnc$^{(neg)}$/eFtn$^{(pos)}$ (b) and the eEnc$^{(neg)}$/CeFtn$^{(pos)}$ (c) crystals.

Since the eEnc$^{(neg)}$/CeFtn$^{(pos)}$ crystal features an *fcc*-derived ordered structure, crystal twinning is expected, as observed in some studies on the Cu$_3$Au ordered structure.[62,63] By calculating the correlation positions between two twinned grains, the previously unexplained correlation peaks in the CCF map are now resolved (Figure S4b, Supporting Information), providing evidence for the presence of twin domains in the eEnc$^{(neg)}$/CeFtn$^{(pos)}$ crystal. Twinning in an *fcc* structure typically occurs when the stacking sequence of the close-packed (111) planes is disturbed, resulting in the two twinned grains exhibiting a relative rotation of 60° around one of the equivalent [111] twin axes, indicating the Σ3 twinning.
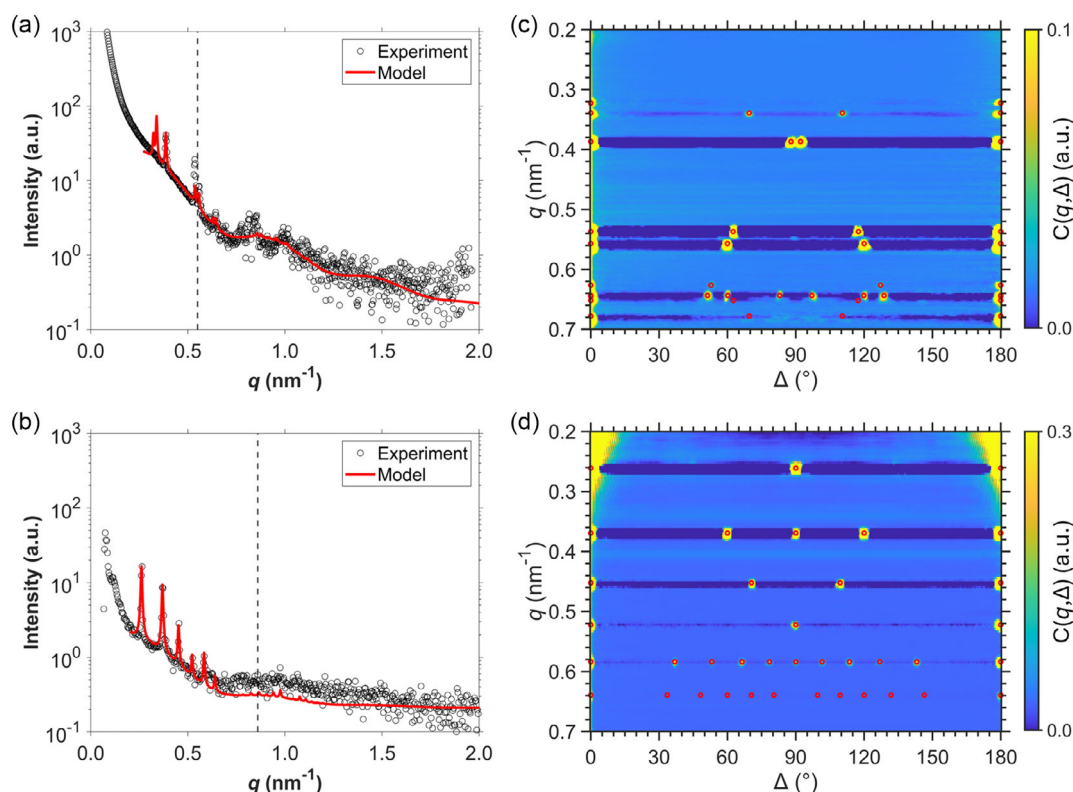
Figure 8. a,b) Radial intensity profiles for the eEnc$^{(neg)}$@AuEnc$^{(neg)}$ (a) and the AuEnc$^{(neg)}$/eFtn$^{(pos)}$@eEnc$^{(neg)}$/eFtn$^{(pos)}$ (b) crystals. They are shown on a logarithmic scale as a function of the scattering vector magnitude, q. Experimental data are shown as black circles, and the vertical dashed line marks the maximum extent of the full q-circle ($q_{full} = q_x = q_y$) that can be captured by the detector. c,d) Correlation maps $C(q, \Delta)$ are displayed for the eEnc$^{(neg)}$@AuEnc$^{(neg)}$ crystal with a q-step size of 0.0023 nm^{-1} (c) and for the AuEnc$^{(neg)}$/eFtn$^{(pos)}$@eEnc$^{(neg)}$/eFtn$^{(pos)}$ crystal with a q-step size of 0.0037 nm^{-1} (d). The correlated positions (g_{hkl}, Δ_g) are calculated from the model lattice and marked as red circles in the correlation maps. The nanoparticle superlattice in the eEnc$^{(neg)}$@AuEnc$^{(neg)}$ crystal exhibits a simple tetragonal structure, while the AuEnc$^{(neg)}$/eFtn$^{(pos)}$@eEnc$^{(neg)}$/eFtn$^{(pos)}$ crystal exhibits a simple cubic structure. Based on the determined unit cell parameters and the predicted nanoparticle arrangement, the radial intensity profiles were calculated and shown as red lines in the left panels.

ADVANCED
SCIENCE NEWS
www.advancedsciencenews.com

**small
structures**
www.small-structures.com

Furthermore, consistent with the coordination numbers of protein cages in the CeFtn[(neg)] and AuEnc[(neg)] crystals, each cage in the binary protein-nanoparticle composite is coordinated by twelve neighboring cages. In the CeFtn[(neg)]/eFtn[(pos)] crystal, each cage coordinates with four like-charged cages and eight oppositely charged cages, while in the AuEnc[(neg)]/eFtn[(pos)] and eEnc[(neg)]/CeFtn[(pos)] crystals, each cage coordinates with four cages of the same type and eight of a different type.

2.4. Protein-Nanoparticle Composites with Core-Shell Morphology

Two additional biohybrid supercrystals with core-shell morphology were investigated: (i) eEnc[(neg)]@AuEnc[(neg)] and (ii) AuEnc[(neg)]/eFtn[(pos)]@eEnc[(neg)]/eFtn[(pos)] (core@shell) crystals. These crystals share similar constituents with their parent crystals, AuEnc[(neg)] and AuEnc[(neg)]/eFtn[(pos)], respectively. The core-shell crystals were prepared by using the core crystal as a seed for the subsequent growth of the shell. Microscopy images of these supercrystals reveal distinct contrast, distinguishing regions left empty from those loaded with nanoparticles. The superlattice structure of both core-shell crystals was investigated in comparison to their parent crystals. Orientational-averaging the 3D intensity distribution generates the radial intensity profiles of both core-shell crystals, shown as black circles in **Figure 8**a,b.

To determine the unit cell parameters, the angular CCFs were calculated and stacked into correlation maps for the eEnc[(neg)]@AuEnc[(neg)] (Figure 8c) and the AuEnc[(neg)]/eFtn[(pos)]@eEnc[(neg)]/eFtn[(pos)] crystals (Figure 8d). The determined parameters of the core-shell crystals are summarized in **Table 3**, revealing structural similarities to their respective parent crystals. In the eEnc[(neg)]@AuEnc[(neg)] crystal, AuNPs encapsulated in the encapsulin cages assemble into a primitive rhombohedral superlattice with unit cell parameters $a_R = 23.44$ nm and $\alpha_R = 57.55°$. This structure transforms into a rhombohedral-centered lattice with hexagonal axes, where a_{HR} is 22.57 nm and c_{HR} is 58.46 nm, yielding a packing factor of 0.70 that closely matches that of the parent homogeneous AuEnc[(neg)] crystal. Similarly, in the AuEnc[(neg)]/eFtn[(pos)]@eEnc[(neg)]/eFtn[(pos)] crystal, the AuNPs within the encapsulin cages organized into a simple cubic superlattice characterized by a unit cell parameter $a_L = 24.07$ nm, closely resembling the parent AuEnc[(neg)]/eFtn[(pos)] crystal.

The unit cell parameters were then used to calculate the radial intensity profiles and compared with the experimental data, as shown by the red lines for the eEnc[(neg)]@AuEnc[(neg)] (Figure 8a) and AuEnc[(neg)]/eFtn[(pos)]@eEnc[(neg)]/eFtn[(pos)] crystals (Figure 8b). Notably, the first two diffraction peaks appear weak in the experimental radial intensity profile of the eEnc[(neg)]@AuEnc[(neg)] crystal. In contrast, the angular correlations between the Bragg peaks in these first two families are captured in the correlation map (Figure 8c), facilitating unit cell determination. Overall, these results suggest that the development of core-shell morphology does not alter the assembly pattern of the nanocages into superlattices, regardless of whether they are loaded or empty. This demonstrates the versatility of morphological control in designing biohybrid supercrystals.

3. Conclusion

In summary, this study provides a comprehensive investigation of the structural properties and assembly behavior of biohybrid supercrystals composed of protein cages and nanoparticles. We examined various composite systems, including homobinary and heterobinary composites, as well as supercrystals with core-shell morphology. In contrast to the approaches that rely on ensemble diffraction from a collection of multiple crystals, in the current work, we collected diffraction data from the individual biohybrid crystals in the small-angle X-ray regime. This allows us to demonstrate the feasibility of using AXCCA for structural determination of biohybrid supercrystals and to analyze superlattice structure through radial intensity profiles. This enables the determination of nanoparticle arrangements within the unit cell.

This work presents an approach for determining the structure of protein cage assemblies containing encapsulated nanoparticles. The method shown in the current study is complementary to the use of SAXD data for superlattice structure refinement in reciprocal space and electron cryo-tomography for structure determination in direct space.[30] Furthermore, we identified the structure of a new type of unitary assembly of the encapsulin nanocages filled with AuNPs. Moreover, we showed that the ability to control the morphology of the micron-sized biohybrid crystals while preserving the protein cage assembly pattern is similar to that of their parent homogenous crystals. This opens new possibilities for designing supercrystals with tailored properties for advanced applications.

Using AXCCA, we also observed evidence of twin domains in the biohybrid supercrystals. Overall, the matrix based on protein nanocages offers a versatile scaffold for the precise assembly of inorganic nanoparticles, providing greater flexibility in selecting materials for nanoparticle cargo within protein cages. This study enhances our understanding of the superlattice structures and associated defects in the biohybrid supercrystals, offering new opportunities for designing and engineering diverse biohybrid superlattice architectures.

4. Experimental Section

Assembly of Biohybrid Supercrystals: Several types of biohybrid supercrystals composed of protein nanocages and nanoparticles were prepared. In general, crystals were grown using a hanging drop vapor diffusion setup,

Table 3. Structural parameters for the eEnc[(neg)]@AuEnc[(neg)] and AuEnc[(neg)]/eFtn[(pos)]@eEnc[(neg)]/eFtn[(pos)] crystals obtained through the AXCCA. The mean values of the unit cell parameters for the nanoparticle superlattices were refined from the AXCCA, with the error bars representing the standard deviation determined by the Williamson–Hall method.

Sample name	eEnc[(neg)]@AuEnc[(neg)]	AuEnc[(neg)]/eFtn[(pos)]@eEnc[(neg)]/eFtn[(pos)]
Unit cell length, a_R or a_L [nm]	23.44 ± 0.27	24.07 ± 0.37
Unit cell angle, α_R or α_L [°]	57.55 ± 1.58	90.00 ± 0.80
Nearest neighbor distance between two encapsulins, $d_{NN,\,Enc}$ [nm]	22.57 ± 0.26	24.07 ± 0.38
Type of unit cell	rhombohedral	simple cubic

ADVANCED
SCIENCE NEWS
www.advancedsciencenews.com

small
structures
www.small-structures.com

similar to the crystallization of proteins.[64] The preparation of the protein cages as well as the encapsulation of nanoparticles or synthesis of nanoparticles inside the cages was described in the Supporting Information. The specific assembly procedures for each type of supercrystal were detailed as follows.

CeFtn[(neg)]: For the unitary protein-nanoparticle composite, crystals composed of negatively charged ferritin cages loaded with CeO_2 NPs were prepared as described in previous work.[20] Here, 2 µL of the crystallization solution, which consists of 0.1 M Tris pH 8.5 and 0.52 M magnesium acetate solution, was mixed with 1 µL 50 mM Tris pH 7.5 1 M NaCl and 1 µL negatively charged ferritin cages loaded with CeO_2 NPs (at 4 mg mL^{-1}) in 50 mM Tris pH 7.5 0.3 M NaCl.

AuEnc[(neg)]: Another type of unitary protein-nanoparticle composite, consisting of negatively charged encapsulin cages loaded with AuNPs, was prepared. At 303 K, 1 µL of protein nanocages loaded with AuNPs (6 mg mL^{-1}) in buffer (20 mM Tris pH 7.5, 0.3 M NaCl) were mixed with 1 µL crystallization solution, which consists of 0.2 M calcium acetate, 0.1 M MES pH 6.0%, and 4% (v/v) isopropanol. The elevated temperature was necessary to ensure that the building blocks crystallize in a homogeneous crystal morphology.

For the preparation of a binary protein-nanoparticle composite, two types of protein matrices were used. One type of matrix consisted of two oppositely charged ferritin cages, whereas the other matrix was composed of negatively charged encapsulin cages and positively charged ferritin cages.

CeFtn[(neg)]/*eFtn*[(pos)]: For the sample using the binary ferritin matrix, the negatively charged ferritin cages were loaded with CeO_2 NPs. Crystallization of this sample with empty, positively charged ferritin cages was carried out by mixing 1 µL of each protein cage solution with 2 µL of crystallization solution, which consists of 0.19 M magnesium formate solution, similar to previous work.[28]

AuEnc[(neg)]/*eFtn*[(pos)] and *eEnc*[(neg)]/*CeFtn*[(pos)]: For the crystals formed by the binary encapsulin/ferritin matrix, either the encapsulin cages were loaded with AuNPs or the ferritin cages were loaded with CeO_2 NPs, respectively. These two types of crystals were prepared as described previously.[30] The crystallization drops were prepared with a volume of 4 µL, composed of 2:1:1 crystallization solution, Ftn[(pos)], and Enc[(neg)]. Solutions were added to the droplet in this specific order. The crystallization condition contained 0.16 M ammonium sulfate, whereas the protein concentrations were 4 mg mL^{-1} each, with proteins in buffer solution (encapsulin: 20 mM Tris, pH 7.5, 0.3 M NaCl; ferritin: 50 mM Tris, pH 7.5, 1.0 M NaCl).

To synthesize core-shell crystals (referred to as the eEnc[(neg)]@ AuEnc[(neg)] and AuEnc[(neg)]/eFtn[(pos)]@eEnc[(neg)]/eFtn[(pos)]), in the first step, the core part of the crystal was grown as described above. In the second step, these crystals were transferred to a fresh crystallization drop, containing protein cages (loaded with nanoparticles, if required).

To stabilize the crystals, the samples were crosslinked. A fresh stock solution of sulfosuccinimidyll-4-(N-maleimidomethyl)cyclohexan-1-carboxylate (sulfo-SMCC, 4.8 mg mL^{-1}) was prepared with ultrapure water. The cover slide was briefly removed and 100 µL of the stock solution was added to the crystallization condition and mixed. Depending on the crystal drop size, half the volume of the drop was taken from the mixed reservoir and added for crystal crosslinking. The well was sealed with the cover slide, and crystals were crosslinked for 16 h at 293 K.

X-ray Scattering Experiment: The synchrotron X-ray scattering experiment was conducted at in situ X-ray diffraction and imaging beamline P23 at PETRA III (DESY, Hamburg), with its schematic layout shown in Figure 3. Monochromatic X-rays with a photon energy of 12.5 keV (wavelength = 0.992 Å) were used. The crystals were first transferred into a solution containing the crystallization condition, supplemented with 25% glycerol for cryoprotection, mounted on a MiTegen polymer tip, flash-frozen in liquid nitrogen, and placed on the sample rotation stage, which continuously rotated around the vertical axis over an angular range of 180° at an angular speed of 0.25°/s. The signal from the sample crystals was recorded by a downstream X-Spectrum Lambda 750 K GaAs detector with a pixel size of 55 × 55 µm^2. The scattered X-rays were then collected by the area detector at an acquisition frequency of 1 Hz (corresponding to a frame exposure of 1 s per 0.25°). Measurements were performed at two

different sample-to-detector distances, 0.9 and 1.5 m, to ensure sufficient q-range coverage for the experiment (see Supporting Information). The X-ray beam size was set using slits to dimensions of 100 µm (V) × 100 µm (H) at SDD of 0.9 m and 250 µm (V) × 250 µm (H) at SDD of 1.5 m. During the experiment, the sample crystal was cooled to 100 K using a liquid nitrogen cryojet to mitigate radiation damage to the protein nanocages, thereby maintaining the crystal structure throughout the continuous measurement. The collected 2D scattering patterns over the whole angular range were air-background subtracted and interpolated onto a 3D orthonormal grid with the cubic voxel length of 0.0037 nm^{-1} at SDD of 0.9 m and 0.0023 nm^{-1} at SDD of 1.5 m. Notably, the rectangular array shape of the detector restricted the collection of a complete set of diffraction peaks to within the full q-sphere, restricted by the short axis of the detector (see Supporting Information for more details).

Angular X-ray Cross-Correlation Analysis: AXCCA was utilized to investigate the structure of the biohybrid crystals composed of protein-nanoparticle building blocks. This analysis involved calculating the angular cross-correlation functions between pairs of scattered intensities in 3D reciprocal space[45]

$$C(q, \Delta) = \left\langle \widetilde{I}(\boldsymbol{q}_1)\widetilde{I}(\boldsymbol{q}_2)\delta\left(\frac{\boldsymbol{q}_1 \cdot \boldsymbol{q}_2}{|\boldsymbol{q}_1||\boldsymbol{q}_2|} - \cos\Delta\right)\right\rangle \quad (1)$$

where $\widetilde{I}(\boldsymbol{q}_1)$ and $\widetilde{I}(\boldsymbol{q}_2)$ represents the normalized intensities corresponding to the scattering vectors $\boldsymbol{q}_1$ and $\boldsymbol{q}_2$, respectively. The symbol Δ denotes the relative angle between these vectors, and $\delta(x)$ represents the Kronecker delta function. The averaging $\langle...\rangle$ was performed over all pairs of intensities for which the corresponding scattering vectors satisfy $|\boldsymbol{q}_1| = |\boldsymbol{q}_2| = q$. The intensity $I(\boldsymbol{q})$ was normalized to its mean intensity as follows

$$\widetilde{I}(\boldsymbol{q}) = \frac{I(\boldsymbol{q}) - \langle I(\boldsymbol{q})\rangle}{\langle I(\boldsymbol{q})\rangle} \quad (2)$$

Detailed procedures for unit cell determination of the superlattice structure are provided in the Supporting Information. Additionally, the deviation of the unit cell parameters was determined using the Williamson–Hall method (see Supporting Information).[47,65]

Supporting Information

Supporting Information is available from the Wiley Online Library or from the author.

Acknowledgements

Conflict of Interest

The authors declare no conflict of interest.

Author Contributions

Kuan Hoon Ngoi: formal analysis (lead); investigation (lead); software (lead); conceptualization (lead); data curation (lead); writing—original draft (lead); writing—review and editing (lead). **Laurin Lang**: conceptualization (lead); data curation (lead); investigation (lead); writing—review and editing (equal). **Young Yong Kim**: data curation (lead); investigation (lead). **Niklas Mucke**: data curation (equal); investigation (equal). **Gerard N. Hinsley**: data curation (equal); investigation (equal); writing—review and editing (equal). **Dongwon Kim**: data curation (equal); investigation (equal). **Michael Rütten**: data curation (equal); investigation (equal). **Maximilian Ruffer**: data curation (equal); investigation (equal). **Varnika Yadav**: data curation (equal); investigation (equal). **Henrike Wagler**: data curation (equal); investigation (equal). **Tobias Katenkamp**: data curation (equal); investigation (equal). **Markus Perbandt**: data curation (equal); investigation (equal). **Azat Khadiev**: data curation (lead); investigation (lead); methodology (lead); resources (lead). **Dmitri Novikov**: data curation (lead); investigation (lead); methodology (lead); resources (lead). **Tobias Beck**: conceptualization (lead); data curation (lead); funding acquisition (lead); investigation (lead); supervision (lead); writing—original draft (lead); writing—review and editing (lead). **Ivan A. Vartanyants**: conceptualization (lead); data curation (lead); investigation (lead); supervision (lead); writing—original draft (lead); writing—review and editing (lead).

Data Availability Statement

The data that support the findings of this study are available from the corresponding author upon reasonable request.

Keywords

[1] M. A. Boles, M. Engel, D. V. Talapin, *Chem. Rev.* **2016**, *116*, 11220.
[2] K. J. Si, Y. Chen, Q. Shi, W. Cheng, *Adv. Sci.* **2018**, *5*, 1700179.
[3] N. Liu, H. Guo, L. Fu, S. Kaiser, H. Schweizer, H. Giessen, *Nat. Mater.* **2008**, *7*, 31.
[4] D. Nykypanchuk, M. M. Maye, D. Van Der Lelie, O. Gang, *Nature* **2008**, *451*, 549.
[5] S. Y. Park, A. K. R. Lytton-Jean, B. Lee, S. Weigand, G. C. Schatz, C. A. Mirkin, *Nature* **2008**, *451*, 553.
[6] R. J. Macfarlane, B. Lee, M. R. Jones, N. Harris, G. C. Schatz, C. A. Mirkin, *Science* **2011**, *334*, 204.
[7] W. Liu, M. Tagawa, H. L. Xin, T. Wang, H. Emamy, H. Li, K. G. Yager, F. W. Starr, A. V. Tkachenko, O. Gang, *Science* **2016**, *351*, 582.
[8] M. E. Leunissen, C. G. Christova, A.-P. Hynninen, C. P. Royall, A. I. Campbell, A. Imhof, M. Dijkstra, R. Van Roij, A. Van Blaaderen, *Nature* **2005**, *437*, 235.
[9] A. M. Kalsin, M. Fialkowski, M. Paszewski, S. K. Smoukov, K. J. M. Bishop, B. A. Grzybowski, *Science* **2006**, *312*, 420.
[10] E. V. Shevchenko, D. V. Talapin, N. A. Kotov, S. O'Brien, C. B. Murray, *Nature* **2006**, *439*, 55.
[11] S. Asakura, F. Oosawa, *J. Polym. Sci.* **1958**, *33*, 183.
[12] R. Nag, N. Rouvière, J. G. Trazo, J. Marcone, N. Kutalia, C. Goldmann, M. Impéror-Clerc, D. Alloyeau, D. Constantin, C. Hamon, *Nano Lett.* **2024**, *24*, 16368.
[13] M. L. Flenniken, M. Uchida, L. O. Liepold, S. Kang, M. J. Young, T. Douglas, *Viruses and Nanotechnology* (Eds: M. Manchester, N.F. Steinmetz), Springer Berlin Heidelberg, Berlin, Heidelberg **2009**, pp. 71–93.
[14] M. Sutter, D. Boehringer, S. Gutmann, S. Günther, D. Prangishvili, M. J. Loessner, K. O. Stetter, E. Weber-Ban, N. Ban, *Nat. Struct. Mol. Biol.* **2008**, *15*, 939.
[15] Y. Zhang, B. P. Orner, *IJMS* **2011**, *12*, 5406.
[16] M. Uchida, M. L. Flenniken, M. Allen, D. A. Willits, B. E. Crowley, S. Brumfield, A. F. Willis, L. Jackiw, M. Jutila, M. J. Young, T. Douglas, *J. Am. Chem. Soc.* **2006**, *128*, 16626.
[17] O. Kasyutich, A. Ilari, A. Fiorillo, D. Tatchev, A. Hoell, P. Ceci, *J. Am. Chem. Soc.* **2010**, *132*, 3621.
[18] G. J. Bedwell, Z. Zhou, M. Uchida, T. Douglas, A. Gupta, P. E. Prevelige, *Biomacromolecules* **2015**, *16*, 214.
[19] M. Künzle, J. Mangler, M. Lach, T. Beck, *Nanoscale* **2018**, *10*, 22917.
[20] M. Künzle, T. Eckert, T. Beck, *Inorg. Chem.* **2018**, *57*, 13431.
[21] E. Simsek, M. Akif Kilic, *J. Magn. Magn. Mater.* **2005**, *293*, 509.
[22] M. Khoshnejad, H. Parhiz, V. V. Shuvaev, I. J. Dmochowski, V. R. Muzykantov, *J. Control. Release* **2018**, *282*, 13.
[23] M. Budiarta, S. Roy, T. Katenkamp, N. Feliu, T. Beck, *Small* **2023**, *19*, 2205606.
[24] S. Bhaskar, S. Lim, *NPG Asia Mater.* **2017**, *9*, e371.
[25] B. Ahn, S. Lee, H. R. Yoon, J. M. Lee, H. J. Oh, H. M. Kim, Y. Jung, *Angew. Chem.* **2018**, *57*, 2909.
[26] N. P. King, J. B. Bale, W. Sheffler, D. E. McNamara, S. Gonen, T. Gonen, T. O. Yeates, D. Baker, *Nature* **2014**, *510*, 103.
[27] R. Divine, H. V. Dang, G. Ueda, J. A. Fallas, I. Vulovic, W. Sheffler, S. Saini, Y. T. Zhao, I. X. Raj, P. A. Morawski, M. F. Jennewein, L. J. Homad, Y.-H. Wan, M. R. Tooley, F. Seeger, A. Etemadi, M. L. Fahning, J. Lazarovits, A. Roederer, A. C. Walls, L. Stewart, M. Mazloomi, N. P. King, D. J. Campbell, A. T. McGuire, L. Stamatatos, H. Ruohola-Baker, J. Mathieu, D. Veesler, D. Baker, *Science* **2021**, *372*, eabd9994.
[28] M. Künzle, T. Eckert, T. Beck, *J. Am. Chem. Soc.* **2016**, *138*, 12731.
[29] L. Lang, H. Böhler, H. Wagler, T. Beck, *Biomacromolecules* **2024**, *25*, 177.
[30] M. Rütten, L. Lang, H. Wagler, M. Lach, N. Mucke, U. Laugks, C. Seuring, T. F. Keller, A. Stierle, H. M. Ginn, T. Beck, *ACS Nano* **2024**, *18*, 25325.
[31] M. A. Kostiainen, P. Hiekkataipale, A. Laiho, V. Lemieux, J. Seitsonen, J. Ruokolainen, P. Ceci, *Nat. Nanotechnol.* **2013**, *8*, 52.
[32] V. Liljeström, J. Mikkilä, M. A. Kostiainen, *Nat. Commun.* **2014**, *5*, 4445.
[33] M. Uchida, K. McCoy, M. Fukuto, L. Yang, H. Yoshimura, H. M. Miettinen, B. LaFrance, D. P. Patterson, B. Schwarz, J. A. Karty, P. E. Prevelige, B. Lee, T. Douglas, *ACS Nano* **2018**, *12*, 942.
[34] T. T. Pham, S. Abe, K. Date, K. Hirata, T. Suzuki, T. Ueno, *Nano Lett.* **2023**, *23*, 10118.
[35] Y. Zhou, A. Shaukat, J. Seitsonen, C. Rigoni, J. V. I. Timonen, M. A. Kostiainen, *Adv. Sci.* **2024**, *11*, 2408416.
[36] M. Uchida, N. E. Brunk, N. D. Hewagama, B. Lee, P. E. Prevelige, V. Jadhao, T. Douglas, *ACS Nano* **2022**, *16*, 7662.
[37] K. Han, Z. Zhang, F. A. Tezcan, *J. Am. Chem. Soc.* **2023**, *145*, 19932.
[38] K. M. Landy, K. J. Gibson, R. R. Chan, J. Pietryga, S. Weigand, C. A. Mirkin, *ACS Nano* **2023**, *17*, 6480.
[39] M. Lach, C. Strelow, A. Meyer, A. Mews, T. Beck, *ACS Appl. Mater. Interfaces* **2022**, *14*, 10656.
[40] N. O. Junker, A. Lindenau, M. Rütten, M. Lach, A. Nedilko, D. N. Chigrin, G. Von Plessen, T. Beck, *Adv. Funct. Mater.* **2023**, *33*, 2303260.
[41] M. Lach, M. Rütten, T. Beck, *Protein Sci.* **2024**, *33*, e5153.

[42] P. Wochner, C. Gutt, T. Autenrieth, T. Demmer, V. Bugaev, A. D. Ortiz, A. Duri, F. Zontone, G. Grübel, H. Dosch, *Proc. Natl. Acad. Sci.* **2009**, *106*, 11511.

[43] M. Altarelli, R. P. Kurta, I. A. Vartanyants, *Phys. Rev. B* **2010**, *82*, 104207.

[44] I. Zaluzhnyy, R. Kurta, M. Scheele, F. Schreiber, B. Ostrovskii, I. Vartanyants, *Materials* **2019**, *12*, 3464.

[45] D. Lapkin, A. Shabalin, J.-M. Meijer, R. Kurta, M. Sprung, A. V. Petukhov, I. A. Vartanyants, *IUCrJ* **2022**, *9*, 425.

[46] J. Carnis, F. Kirner, D. Lapkin, S. Sturm, Y. Y. Kim, I. A. Baburin, R. Khubbutdinov, A. Ignatenko, E. Iashina, A. Mistonov, T. Steegemans, T. Wieck, T. Gemming, A. Lubk, S. Lazarev, M. Sprung, I. A. Vartanyants, E. V. Sturm, *Nanoscale* **2021**, *13*, 10425.

[47] D. Lapkin, S. Singh, F. Kirner, S. Sturm, D. Assalauova, A. Ignatenko, T. Wiek, T. Gemming, A. Lubk, K. Müller-Caspary, A. Khadiev, D. Novikov, E. V. Sturm, I. A. Vartanyants, *ChemNanoMat* **2023**, *9*, e202300336.

[48] I. A. Zaluzhnyy, R. P. Kurta, A. André, O. Y. Gorobtsov, M. Rose, P. Skopintsev, I. Besedin, A. V. Zozulya, M. Sprung, F. Schreiber, I. A. Vartanyants, M. Scheele, *Nano Lett.* **2017**, *17*, 3511.

[49] N. Mukharamova, D. Lapkin, I. A. Zaluzhnyy, A. André, S. Lazarev, Y. Y. Kim, M. Sprung, R. P. Kurta, F. Schreiber, I. A. Vartanyants, M. Scheele, *Small* **2019**, *15*, 1904954.

[50] F. Lehmkühler, B. Fischer, L. Müller, B. Ruta, G. Grübel, *J. Appl. Cryst.* **2016**, *49*, 2046.

[51] A. Niozu, Y. Kumagai, T. Nishiyama, H. Fukuzawa, K. Motomura, M. Bucher, K. Asa, Y. Sato, Y. Ito, T. Takanashi, D. You, T. Ono, Y. Li, E. Kukk, C. Miron, L. Neagu, C. Callegari, M. Di Fraia, G. Rossi, D. E. Galli, T. Pincelli, A. Colombo, S. Owada, K. Tono, T. Kameshima, Y. Joti, T. Katayama, T. Togashi, M. Yabashi, K. Matsuda, et al., *IUCrJ* **2020**, *7*, 276.

[52] D. Mendez, H. Watkins, S. Qiao, K. S. Raines, T. J. Lane, G. Schenk, G. Nelson, G. Subramanian, K. Tono, Y. Joti, M. Yabashi, D. Ratner, S. Doniach, *IUCrJ* **2016**, *3*, 420.

[53] S. Förster, A. Timmann, M. Konrad, C. Schellbach, A. Meyer, S. S. Funari, P. Mulvaney, R. Knott, *J. Phys. Chem. B* **2005**, *109*, 1347.

[54] M. Impéror-Clerc, *Interface Focus* **2012**, *2*, 589.

[55] K. G. Yager, Y. Zhang, F. Lu, O. Gang, *J. Appl. Cryst.* **2014**, *47*, 118.

[56] D. Lapkin, N. Mukharamova, D. Assalauova, S. Dubinina, J. Stellhorn, F. Westermeier, S. Lazarev, M. Sprung, M. Karg, I. A. Vartanyants, J.-M. Meijer, *Soft Matter* **2022**, *18*, 1591.

[57] C. Kittel, P. McEuen, *Introduction to Solid State Physics*, John Wiley & Sons, Hoboken **2018**.

[58] B. D. Cullity, S. R. Stock, *Elements of X-ray Diffraction*, Pearson Education Limited, Harlow, Essex **2014**.

[59] S. M. Rupich, E. V. Shevchenko, M. I. Bodnarchuk, B. Lee, D. V. Talapin, *J. Am. Chem. Soc.* **2010**, *132*, 289.

[60] A. J. Senesi, B. Lee, *J. Appl. Cryst.* **2015**, *48*, 1172.

[61] H. Yamaguchi, O. Kitakami, S. Okamoto, Y. Shimada, K. Oikawa, K. Fukamichi, *Appl. Phys. Lett.* **2001**, *79*, 2001.

[62] S. Zang, A. W. Hauser, S. Paul, G. M. Hocky, S. Sacanna, *Nat. Mater.* **2024**, *23*, 1131.

[63] J. G. Antonopoulos, F. W. Schapink, F. D. Tichelaar, *Philos. Mag. Lett.* **1990**, *61*, 195.

[64] M. A. Dessau, Y. Modis, *JoVE* **2011**, 2285.

[65] G. K. Williamson, W. H. Hall, *Acta Metall.* **1953**, *1*, 22.